REPORT

www.the-innovation.org

Retinomorphic X-ray detection using perovskite with hydrion-conductive organic cations

Hang Yin,[1] Jincong Pang,[1] Shan Zhao,[1] Haodi Wu,[1] Zihao Song,[1] Xing Li,[3] Zhiping Zheng,[1,2] Ling Xu,[1,2] Jiang Tang,[1,2] and Guangda Niu[1,2,4,*]
*Correspondence: guangda_niu@hust.edu.cn

Received: February 20, 2024; Accepted: June 3, 2024; Published Online: June 5, 2024; https://doi.org/10.1016/j.xinn.2024.100654

GRAPHICAL ABSTRACT

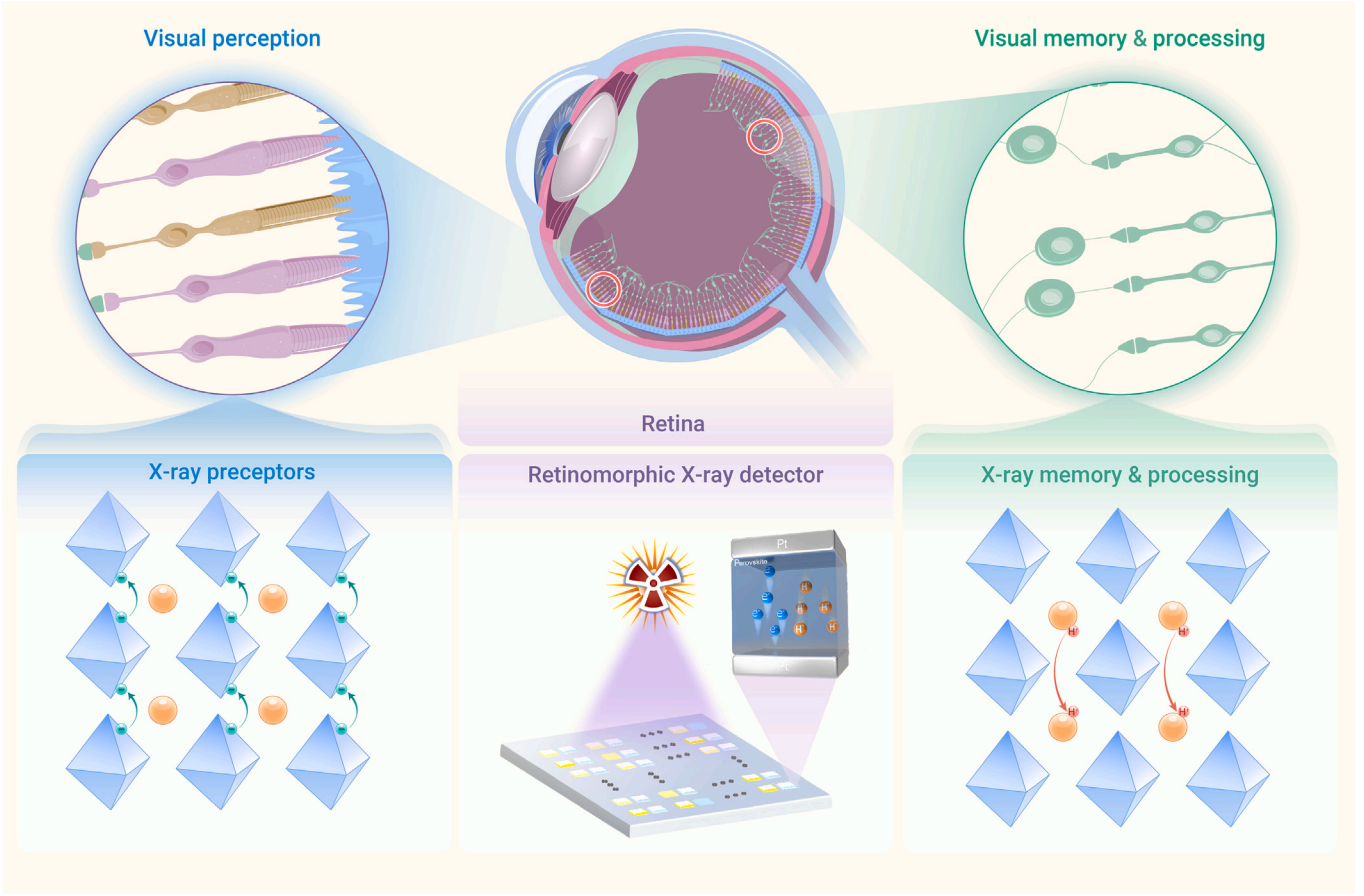

PUBLIC SUMMARY

- Conceptual advance: groundbreaking retinomorphic X-ray detector architecture, in stark contrast to the conventional X-ray detection system with separate detector, memory, and processing modules.
- A remarkable compression ratio of 18.06%, an outstanding recognition accuracy of 98.6%, and a retention time of up to 205 s.
- Opening up new avenues for exploring additional memristor mechanisms and materials within the realm of organic-inorganic hybrid systems.

REPORT

Retinomorphic X-ray detection using perovskite with hydrion-conductive organic cations

Hang Yin,[1] Jincong Pang,[1] Shan Zhao,[1] Haodi Wu,[1] Zihao Song,[1] Xing Li,[3] Zhiping Zheng,[1,2] Ling Xu,[1,2] Jiang Tang,[1,2] and Guangda Niu[1,2,4,*]

[1]Wuhan National Laboratory for Optoelectronics and School of Optical and Electronic Information, Huazhong University of Science and Technology, Wuhan 430074, China

[2]Optical Valley Laboratory, Wuhan 430074, China

[3]Institute of Microelectronics of the Chinese Academy of Sciences, Beijing 100029, China

[4]Research Institute of Huazhong University of science and technology in Shenzhen, Shenzhen 518057, China

*Correspondence: guangda_niu@hust.edu.cn

Received: February 20, 2024; Accepted: June 3, 2024; Published Online: June 5, 2024; https://doi.org/10.1016/j.xinn.2024.100654

Citation: Yin H., Pang J., Zhao S., et al., (2024). Retinomorphic X-ray detection using perovskite with hydrion-conductive organic cations. The Innovation **5(4)**, 100654.

X-ray detection is crucial across various sectors, but traditional techniques face challenges such as inefficient data transmission, redundant sensing, high power consumption, and complexity. The innovative idea of a retinomorphic X-ray detector shows great potential. However, its implementation has been hindered by the absence of active layers capable of both detecting X-rays and serving as memory storage. In response to this critical gap, our study integrates hybrid perovskite with hydrion-conductive organic cations to develop a groundbreaking retinomorphic X-ray detector. This novel device stands at the nexus of technological innovation, utilizing X-ray detection, memory, and preprocessing capabilities within a single hardware platform. The core mechanism underlying this innovation lies in the transport of electrons and holes within the metal halide octahedral frameworks, enabling precise X-ray detection. Concurrently, the hydrion movement through organic cations endows the device with short-term resistive memory, facilitating rapid data processing and retrieval. Notably, our retinomorphic X-ray detector boasts an array of formidable features, including reconfigurable short-term memory, a linear response curve, and an extended retention time. In practical terms, this translates into the efficient capture of motion projections with minimal redundant data, achieving a compression ratio of 18.06% and an impressive recognition accuracy of up to 98.6%. In essence, our prototype represents a paradigm shift in X-ray detection technology. With its transformative capabilities, this retinomorphic hardware is poised to revolutionize the existing X-ray detection landscape.

INTRODUCTION

The strong penetration ability of high-energy X-rays makes them essential for non-destructive analysis. Recently, real-time X-ray detection has garnered significant research interest[1-3] and is crucial for various applications. These include dynamic imaging for medical diagnosis, high-speed detection in security screenings and industrial inspections, and kilohertz to gigahertz X-ray imaging in synchrotron facilities.[4-6] However, conventional X-ray detection systems, which consist of discrete pixel sensing arrays, analog-to-digital converters, memory, and processing modules, suffer from bulkiness, high complexity, and power consumption issues.[7,8] Additionally, the increasing volume of detection data, driven by a higher frame rate, pixels per inch, and bits per pixel, makes data conversion, transmission, storage, and processing extremely challenging.[9] For instance, the data volume of a commercial dynamic flat panel detector can reach 120 gigabits per second (Gbps), which far exceeds the transmission limits (5 Gbps) of universal serial bus 3.0.[10]

The human retina excels in real-time information processing, with rod and cone cells functioning as the sensory layer and horizontal, bipolar, and amacrine cells serving as the storage and processing layer.[11] By combining signal perception, memory, and advanced visual system processing, the retina effectively filters out redundant and unnecessary visual input. This integration significantly reduces data volume and improves the speed of feature extraction and real-time information detection.[12] Implementing a retina-inspired X-ray detector offers a promising solution to the challenge faced by traditional X-ray detectors. However, to our knowledge, retinomorphic X-ray detectors have not yet been explored. The primary obstacle is the absence of active-layer materials that can simultaneously provide X-ray detection and memory capabilities. For instance, commonly used commercial X-ray detection materials, such as CsI scintillators, CdTe semiconductors, and emerging perovskites, cannot be reconfigured as memory components.[3,13,14] Similarly, vision sensors inspired by the retina and developed using ultrathin memristive oxides or two-dimensional chalcogenides encounter challenges in efficiently detecting high-energy X-rays.[15,16]

In this study, we introduce a pioneering approach to X-ray detection inspired by the retina. This involves the development of novel perovskite semiconductors with dual capabilities for both X-ray detection and short-term memory. To facilitate the memory function, we synthesized an organic-inorganic hybrid perovskite semiconductor, 3-APy$_2$BiBr$_6$·H$_2$O, characterized by hydrogen vacancies within the organic amines. These vacancies enable easy proton transport, facilitating resistive memory functionality. Simultaneously, electrons and holes generated by X-ray exposure traverse the metal halide octahedral frameworks, facilitating X-ray detection. These innovative perovskite materials demonstrate a correlation between their X-ray responsiveness and proton conductivity. This correlation resembles synaptic short-term plasticity, providing short-term memory capabilities for information processing.

The assembled detector exhibits distinctive response characteristics to X-ray radiation, presenting long retention times and excellent linearity across various parameters, such as X-ray intensity, number of pulses, and pulse duration. Using interframe differential computations, the retinomorphic X-ray detector accomplishes 100% separation of key information within a motion sequence, leading to a remarkable recognition accuracy of 98.6%. This performance significantly exceeds that of conventional X-ray detection methods. The retinomorphic detector seamlessly integrates X-ray detection, memory, and computing capabilities, potentially offering a paradigm shift in transforming the X-ray detection methodologies through innovative approaches.

RESULT AND DISCUSSION

Figures 1A and 1B depict the operational mechanism of the human retina and the retinomorphic X-ray detection scheme. In the human retina, rod and cone cells detect incident photons and transform them into electrical potential. Following this, the bipolar cells, horizontal cells, ganglion cells, and amacrine cells collectively store and process the signal information, facilitating real-time detection and recognition.[17] Following a comparable framework, our design integrates perovskite with hydrion-conductive organic cations to serve as both the X-ray-sensitive layer and the memristor layer. In our configuration, the retinomorphic X-ray detector adeptly senses X-ray photons and translates them into electrons/holes, mimicking the optical signal reception function of the sensory layer. When subjected to X-ray pulses, the detector produces either a short-term memory positive photo-response (STM-PP) or a negative photo-response (STM-NP), depending on the programmable external bias polarity. This capability reflects the antagonistic shunt and memory function observed in optic nerve cells.[18] Utilizing the antagonistic shunt and memory function, the retinomorphic X-ray detector facilitates real-time X-ray detection. Each pixel within the retinomorphic X-ray detector array consists of two sub-detector units, which are cyclically connected to positive and negative voltages at different time intervals.[19]

We can conceptualize the moving object as a sequence of images captured at different intervals from time t_0 to $t_0+\Delta t$ (Figure 1C). For example, at time t_0, there is a generation of a STM-PP, and the grayscale distribution of the image is denoted as Y_{mn}. Similarly, at time $t_0+\Delta t$, STM-NP are generated, and their grayscale distribution is represented as R_{mn}.

The positive (Y_{mn}) and negative (R_{mn}) short-term memory photo-responses of size m × n are stored at their corresponding time points (Y_{mn} at t_0 and R_{mn} at

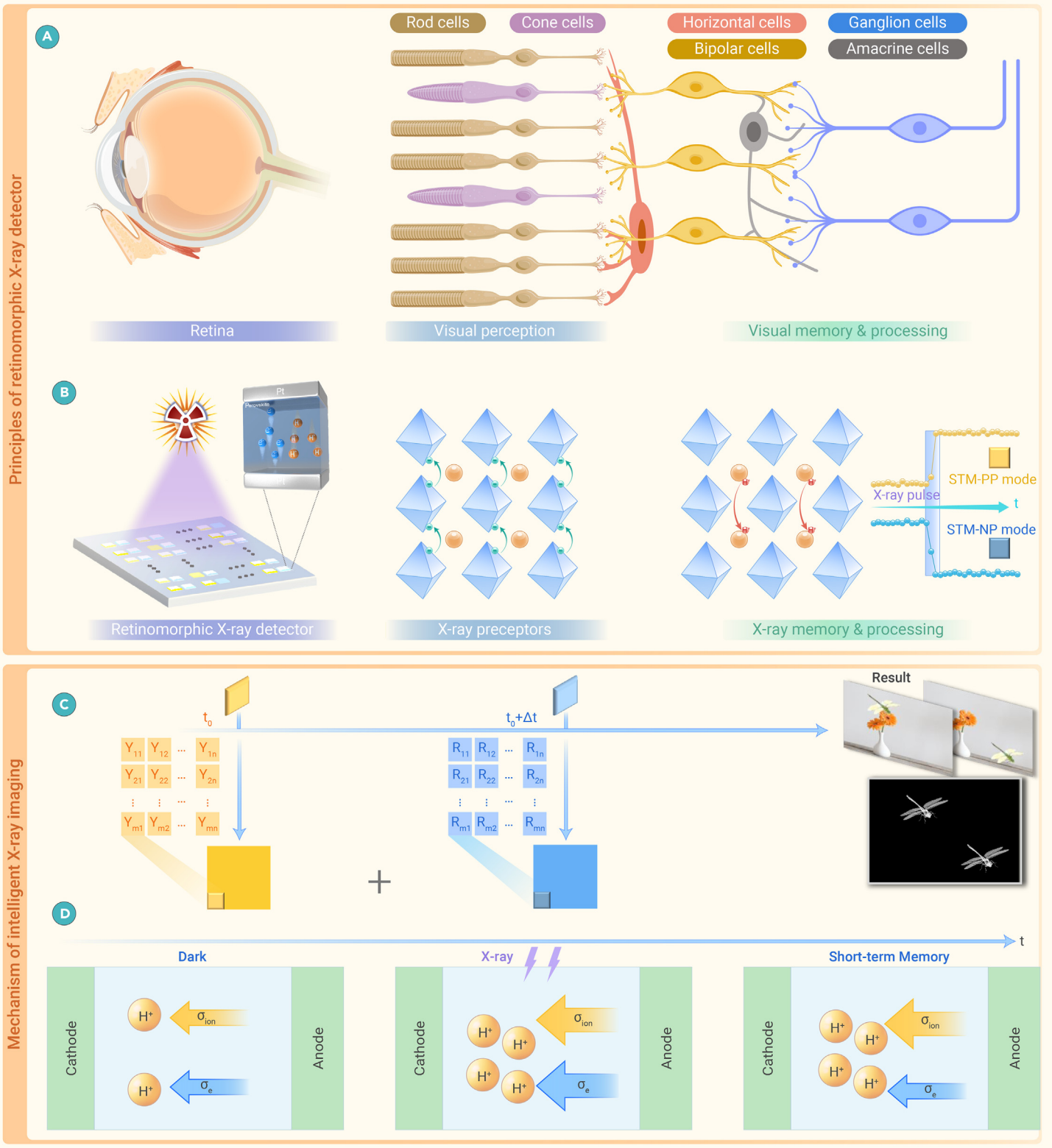

Figure 1. Principles of the retinomorphic X-ray detector and mechanism of intelligent X-ray imaging (A) The functioning principles of the human retina in visual perception. (B) The retinomorphic X-ray detector. This detector's X-ray response from metal halide octahedral skeletons replicates the visual perception functions of rod and cone cells. Simultaneously, proton transport-mediated resistive states simulate the memory functions of bipolar, horizontal, ganglion, and amacrine cells. (C) A schematic of the retinomorphic X-ray detector for advanced X-ray imaging of moving objects. The combined positive and negative pixel arrays yield a processed pixel output, and interframe differential computation (images at t_0 and $t_0+\Delta t$) facilitates the detection of moving objects. (D) A schematic depicting the interaction between X-ray response and proton conductivity.

$t_0+\Delta t$). To process the image, the stored results are added to derive the processed pixel output signal (Equation 1):

$$X_{mn} = Y_{mn} + R_{mn} \quad \text{(Equation 1)}$$

The retinomorphic X-ray detector achieves multiple eye functions by overlaying optical information over time. In situations where there are no moving objects, within a time interval Δt, the pixel array generates a grayscale distribution close to zero. This occurs because the STM-PP and STM-NP matrices have comparable absolute values. During real-time X-ray detection, the static pixels are

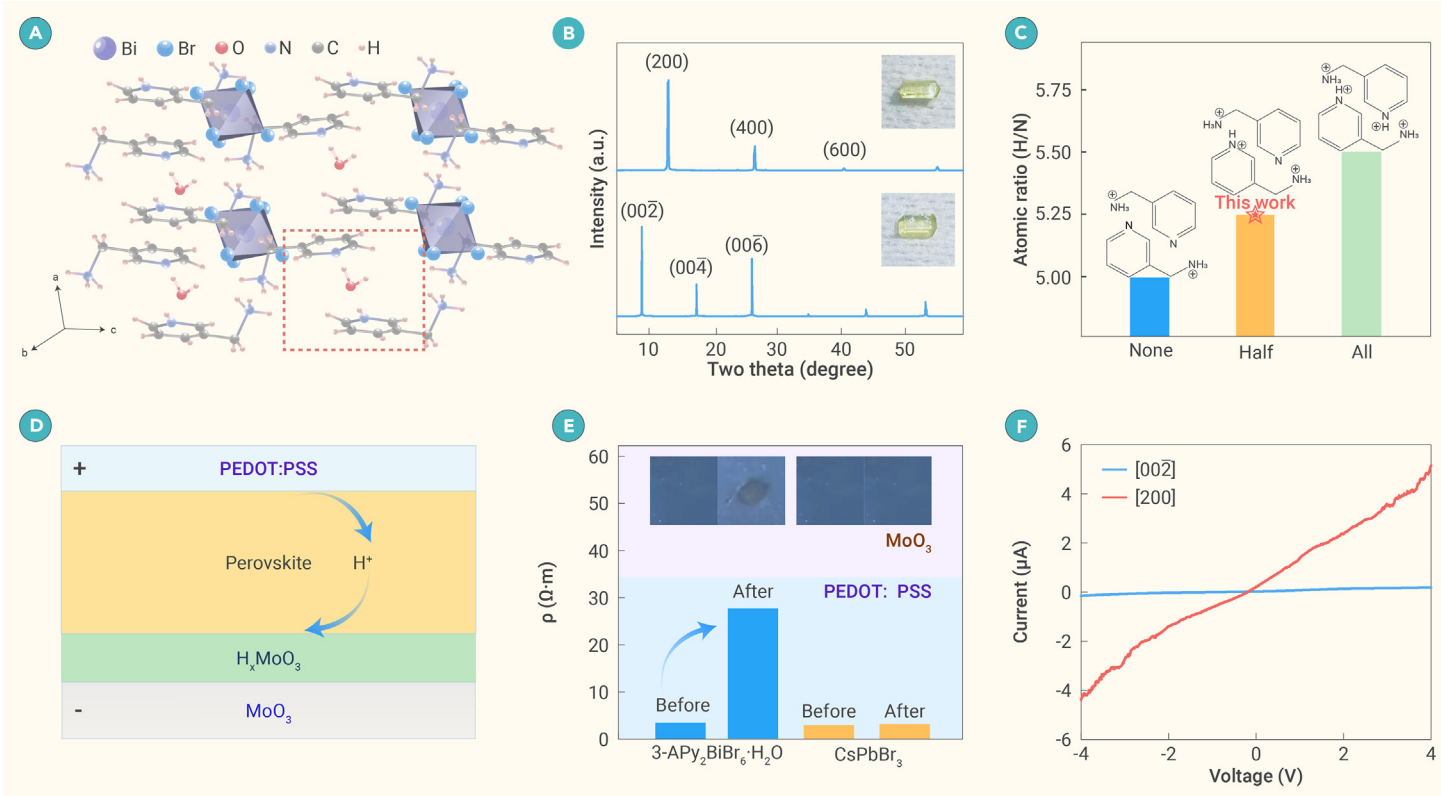

Figure 2. Material characterization of 3-$APy_2BiBr_6·H_2O$ SCs (A) Schematic of the crystal structure of 3-$APy_2BiBr_6·H_2O$ SCs. (B) XRD patterns of 3-$APy_2BiBr_6·H_2O$ crystals at specific orientations. (C) Ratio of hydrogen to nitrogen atoms in 3-$APy_2BiBr_6·H_2O$ SCs across different protonation states. (D) Device configuration used to analyze proton transport properties. (E) Resistivity enhancement of PEDOT:PSS and the color change in the MoO_3 layer upon application of biases. (F) Dark current-voltage characteristics of the crystals along the [200] and [00$\bar{2}$] directions.

disregarded. Conversely, when a moving object is present for the duration of Δt, the array exclusively outputs the moving object, while the stationary background remains unchanged. Leveraging the device's memory function, the absolute values of the STM-PP and STM-NP matrices fluctuate within the moving portion. This discrepancy leads to the summation of grayscale outputs after storing antagonistic results. Compared to conventional real-time X-ray detection technology, the retinomorphic X-ray detector notably simplifies the output image by improving the differentiation between dynamic and static pixels (Figure 1C).

To meet the specified design criteria, it is imperative to investigate novel semiconductor materials. Traditional X-ray detection materials solely detect X-rays without incorporating memristor functionality,[20,21] while optoelectronic synaptic devices struggle to efficiently detect X-rays due to their limited attenuation strength (Figure S1). Halide perovskites have recently emerged as promising semiconductors for X-ray detection owing to their distinctive characteristics. These features encompass a high X-ray attenuation coefficient, a high carrier mobility-lifetime product, a straightforward synthesis process, and compatibility with the integration of front-end circuits.[22,23] While numerous perovskite semiconductor materials have been investigated, the development of perovskite X-ray detectors with retinomorphic capabilities has remained challenging to achieve. However, in this study, we successfully addressed this challenge by synthesizing a novel perovskite variant, 3-$APy_2BiBr_6·H_2O$. This material comprises one Bi^{3+} cation coordinated with six Br^- anions, with 3-(aminomethyl) pyridine (3-APy) and H_2O serving as spacers to separate the metal halide octahedra. 3-APy contains a pyridine ring and an amine group. Remarkably, only half of the pyridine rings are protonated in this structure. The arrangement of organic ions alternates between fully protonated 3-APy ($C_6H_{10}N_2$) and incompletely protonated 3-APy ($C_6H_9N_2$) in the [200] crystal direction (Figure 2A). This configuration results in a distinct structure with numerous H vacancies, facilitating a pathway for H^+ transport. Furthermore, the hydrogen atoms within the fully protonated 3-APy ($C_6H_{10}N_2$) pyridine ring can easily dissociate, producing mobile hydrions that are then transported through the hydrion-conductive channel. This feature sets it apart from nearly all previously reported perovskites, where organic amines are fully protonated.[24] 3-$APy_2BiBr_6·H_2O$ offers distinct pathways for H^+ transport and electron transport, with H^+ transport along H vacancies and electrons traversing the octahedral skeleton. This differentiation in transport pathways is critical for establishing the short-term memory characteristics of retinomorphic X-ray detectors. The overall conductance arises from both ionic (σ_{ion}) and electronic (σ_e) conductance components. Upon exposure to X-ray illumination, the X-ray-generated electrons and holes augment the σ_e value. At the same time, the decrease in activation energy for H^+ mobility promotes increased migration of H^+ within the device, leading to an increase in σ_{ion} (Figure 1D). Previous studies have confirmed the strong coupling between σ_{ion} and σ_e in perovskites.[14,25] Upon returning to the dark state, the value of σ_e quickly returns to its initial level, whereas H^+ migration persists due to its slow diffusion rate. Consequently, the equilibrium value of the dark-state σ_{ion} is influenced by X-ray irradiation, facilitating the integration of short-term memory and X-ray sensing.

Following the outlined design approach, we effectively synthesized 3-$APy_2BiBr_6·H_2O$ perovskite single crystals (SCs) employing a controlled cooling method, as reported under materials and methods and in Figure S2. To ascertain the crystal structure, we performed X-ray diffraction (XRD) analysis (Figure S3) and conducted SC-XRD analysis. The SC-XRD data indicate that 3-$APy_2BiBr_6·H_2O$ SCs crystallize in a monoclinic system, with unit cell dimensions of a = 13.649 Å, b = 8.970 Å, and c = 21.002 Å (Tables S1 and S2). To evaluate the purity and crystalline quality of our crystals, we examined the XRD patterns of various crystal planes, including (200) and (00$\bar{2}$), as depicted in Figure 2B.

The full-width at half-maximum of (00$\bar{2}$) is 0.08°, confirming the exceptional crystallinity of the synthesized crystals. Additionally, the band gap of this material was determined to be 2.75 eV using the Tauc plot method (Figure S4). As depicted in Figures S5 and S6, we conducted density functional theory calculations of this material utilizing the Heyd-Scuseria-Ernzerhof hybrid functional, which incorporates spin-orbit coupling effects. The valence band maximum of this material originates from the antibonding states of Bi 6s and Br 4p orbitals. In contrast, the conduction band minimum is primarily composed of Bi 6p and organic molecular π orbitals. Furthermore, the calculated band gap of this material is 2.53 eV, which closely aligns with the result obtained from the Tauc plot.

To verify the half-protonated structure of the 3-$APy_2BiBr_6·H_2O$ SCs, we conducted an elemental analysis (Table S3). The results revealed that the ratio of

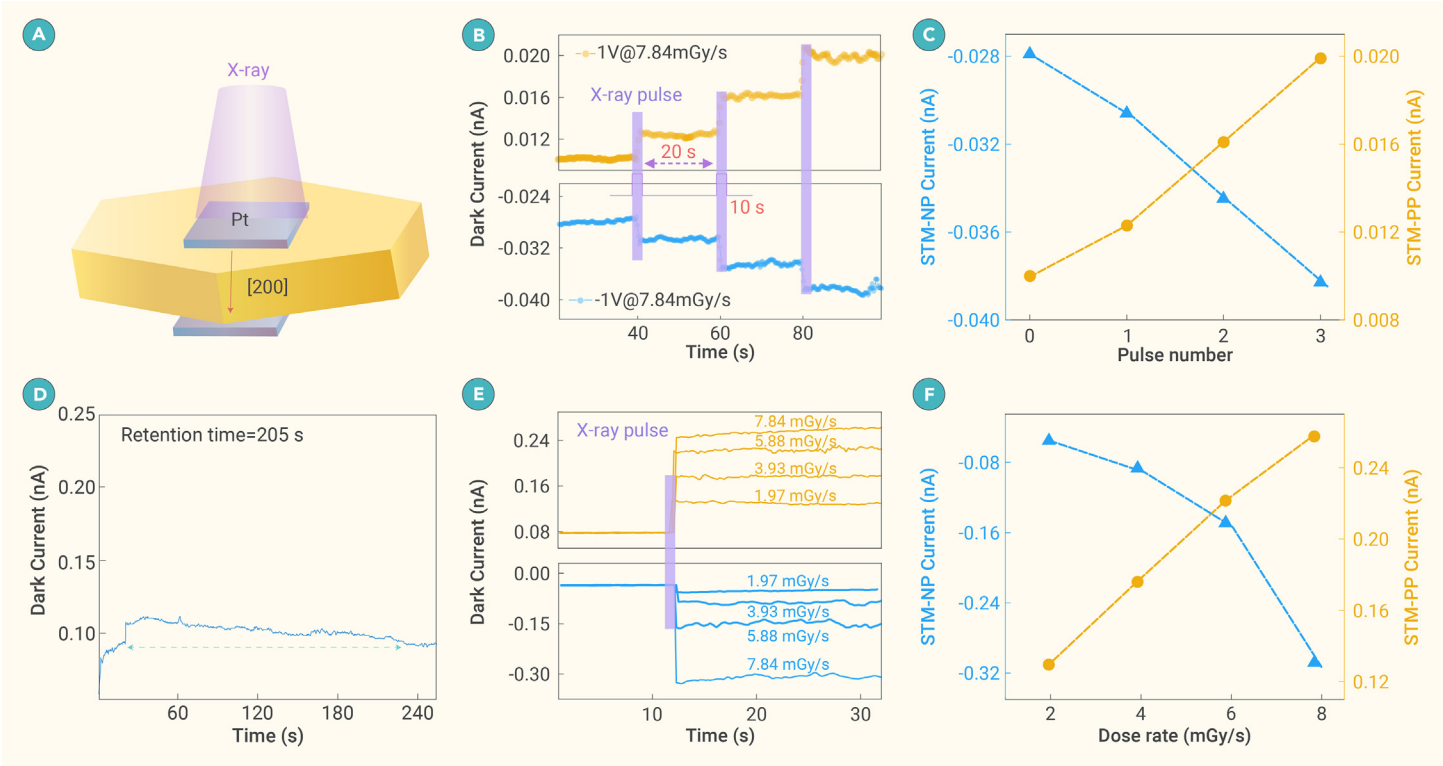

Figure 3. Electrical performance of the retinomorphic X-ray detector (A) Pt electrode aligned with the [200] crystal orientation. (B) Accumulated positive and negative photoconductivity under successive X-ray pulses (duration: 10 s). (C) Linear correlation between STM-PP and STM-NP variations and the number of X-ray pulses. (D) Retention duration of the device after the X-ray pulse is turned off. An X-ray pulse (dose rate: 5.88 mGy s^{-1}) was applied for 15 s. (E) STM-PP and STM-NP curves under varying X-ray intensity modulation, with purple frames indicating the timing of the X-ray pulse (duration: 10 s). (F) Relationship between STM-PP and STM-NP and the X-ray dose rate.

H/N in the sample was 5.253, closely matching the theoretical value of 5.25 for the half-protonated crystal structure ($C_{12}H_{19}N_4BiBr_6 \cdot H_2O$) (Figure 2C). If the crystal structure were fully deprotonated ($C_{12}H_{16}N_4BiBr_6 \cdot H_2O$) or fully protonated ($C_{12}H_{20}N_4BiBr_6 \cdot H_2O$), the theoretical values of H/N would be 5 or 5.5, respectively. Therefore, based on the elemental analysis results indicating an H/N ratio of 5.253, we can deduce that the chemical formula of the as-grown crystal is indeed $C_{12}H_{19}N_4BiBr_6 \cdot H_2O$ (3-$APy_2BiBr_6 \cdot H_2O$).

To further confirm the proton transportation within 3-$APy_2BiBr_6 \cdot H_2O$, we set up a device comprising poly(3,4-ethylenedioxythiophene (PEDOT):poly(4-styrenesulfonate) (PSS)/perovskite/MoO_3 (Figure 2D). We chose PEDOT:PSS and MoO_3 for their proton-sensitive conductivity and color, respectively.[26] More detailed information regarding the fabrication and testing of the device can be found in the supporting information (Figure S7). In this setup, PEDOT:PSS served as the anode. PEDOT is a unique polymer known for its high conductivity and transparency, stability in various environments, and resistivity dependent on the concentration of H^+.[27] Upon applying a bias voltage, H^+ ions move from the anode to the cathode through distinct H^+ transport pathways within the 3-$APy_2BiBr_6 \cdot H_2O$ layer.

Consequently, the H^+ concentration within the PEDOT:PSS layer decreases, causing a 6-fold increase in PEDOT:PSS resistance compared to its initial state (Figures 2E and S8). Additionally, at the cathode end, the MoO_3 layer undergoes a color transformation from colorless to blue. This change in color originates from the injection of H^+ ions from perovskite into MoO_3 during positive voltage scanning, as depicted in Figure 2E, resulting in the generation of a blue-colored oxide, H_xMoO_3.[28] Conversely, $CsPbBr_3$, when subjected to the same device structure, shows no change in resistivity in the PEDOT:PSS anode and no coloration in the MoO_3 cathode. To further confirm that the color change is caused by proton transport, we applied a reverse voltage, which subsequently caused the color to revert (Figure S9).

Additionally, we analyzed the proton transport mechanism. As shown in Figure S10A, two potential pathways for H^+ movement are observed, from a fully protonated 3-APy to an incompletely protonated 3-APy: (1) transfer from site 1 to site 2 along the [200] direction and (2) transfer from site 1 to site 3 along the [00$\bar{2}$] direction. Distance measurements between the three sites reveal that the separation between sites 1 and 2 is 3.70 Å, while the distance between sites 1 and 3 is 12.76 Å. The energy barrier for migration is lower when moving from site 1 to site 2 in the [200] direction, making this pathway more favorable. Moreover, the inclusion of an H_2O molecule as a transfer bridge further facilitates this pathway. Figure S10B illustrates a proposed H^+ diffusion pathway between two adjacent organic molecules through H_2O, known as Grotthuss proton transport.[29] Along this pathway, the H_2O molecule accepts an H^+ ion, forming H_3O^+ via a hydrogen bond with the N atom on the pyridine ring. Following the reverse process of H^+ transfer, H_3O^+ is destabilized and returns to its original state as H_2O, while the N atom on the adjacent pyridine ring acquires the H^+ ion. This pathway exhibits an energy barrier of only 0.14 eV (Figure S11), suggesting that H^+ diffusion occurs with remarkable ease within the structure. This migration leads to a significant difference in resistivity between the [200] direction and other crystal plane directions. Specifically, the [200] direction shows a resistivity of 4.27×10^7 Ω cm, whereas the [00$\bar{2}$] direction exhibits a higher resistivity of 1.36×10^9 Ω cm, as illustrated in Figure 2F. The lower resistivity observed in the [200] direction suggests predominant H^+ migration along this path. Simultaneously, the conduction of H^+ in the [200] direction establishes a stabilized current, as demonstrated in Figure S12. It is important to note that prolonged exposure to unidirectional bias conditions can result in crystal degradation due to the migration of H^+. This degradation is revealed as a reduction in the crystal's memory current (red arrow in Figure S13), posing a challenge for retinomorphic X-ray detectors. However, this issue can be addressed by simply applying a negative bias to restore performance, as indicated by the blue arrow in Figure S13.

Following that, we evaluated the detector's performance concerning X-ray sensing and memory capabilities. In this regard, we chose platinum electrodes because of their strong hydrogen adsorption capability,[30] which facilitates memory retention. In our experiments, when compared to the Au/perovskite/Au configuration, we noticed a more significant hysteresis in the Pt/perovskite/Pt setup. This is attributed to the facile adsorption of hydrogen on Pt electrodes, which consequently enhanced ion migration within the perovskite material (Figure S14). Based on previous analysis confirming the movement of H^+ ions along the [200] direction, we proceeded to fabricate symmetrical Pt electrodes oriented along this orientation (Figure 3A).

In Figure 3B, we can observe the evolving polymorphic positive and negative photoconductivity represented by STM-PP and STM-NP as the number of

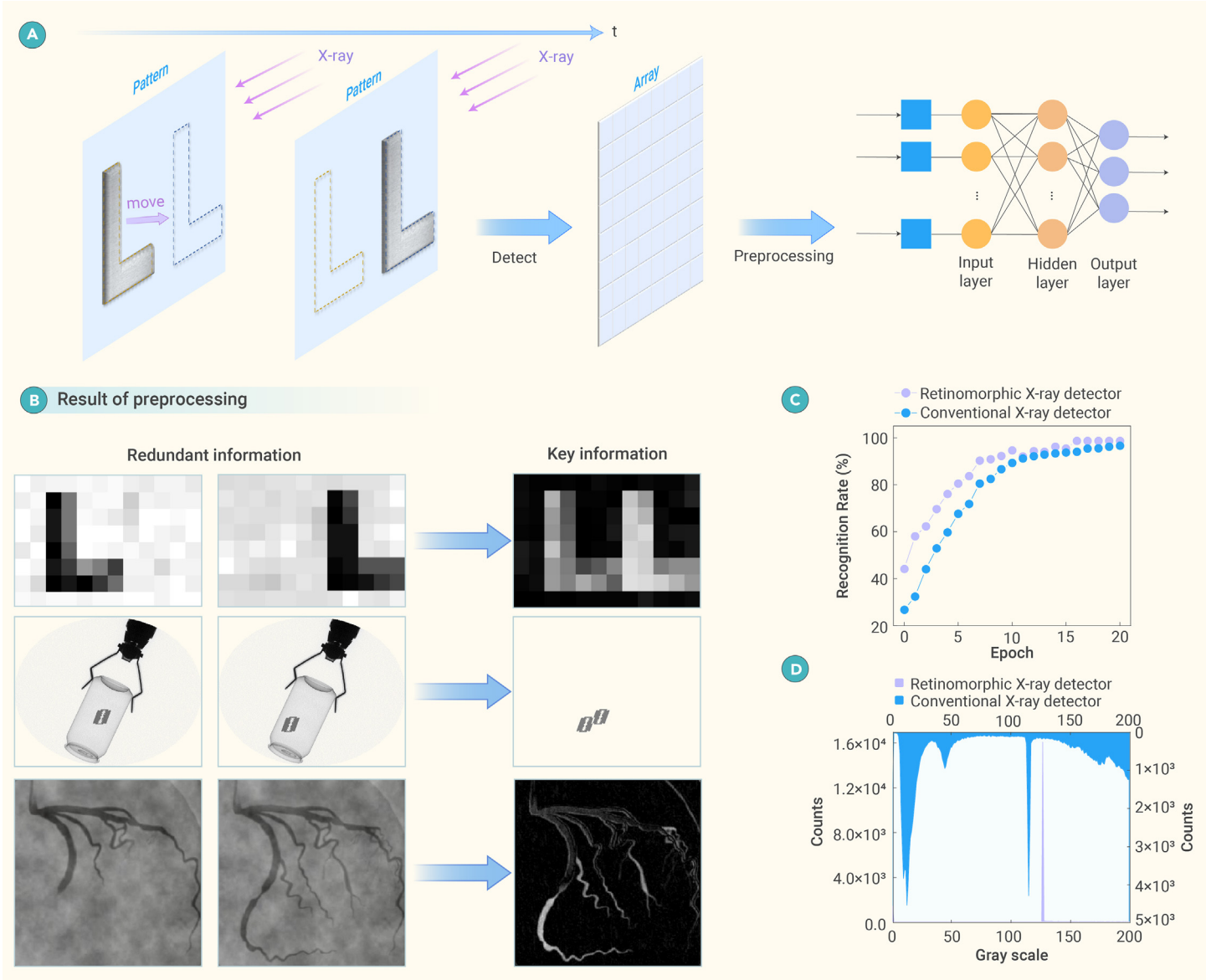

Figure 4. Imaging performance of the retinomorphic X-ray detector (A) Illustration of the retinomorphic X-ray detector used for image preprocessing and an artificial neural network for image recognition. (B) Examples of images before and after preprocessing by the retinomorphic X-ray detector. (C) Comparison of recognition accuracy over epochs using the retinomorphic X-ray detector versus a conventional X-ray detector. (D) Comparison of gray value distribution between the retinomorphic X-ray detector and a conventional X-ray detector.

X-ray pulses gradually increases. The device was exposed to X-rays at a dose rate of 7.84 mGy s^{-1} for 10 s. At a bias of 1 V, the short-term memory dark current showed incremental growth with each subsequent X-ray pulse. Both the STM-PP and STM-NP mode currents demonstrate modulation corresponding to the number of X-ray pulses. Figure 3C presents the results of linear fitting for both STM-PP and STM-NP modes with respect to the pulse count. The determination coefficients R^2 reach high values, up to 0.98811 for STM-PP and 0.99577 for STM-NP, indicating a robust linear relationship. The memory retention period was measured at 205 s, with the X-ray pulse (5.88 mGy s^{-1}) lasting for 15 s (Figure 3D). This retention time is long enough for subsequent imaging processing tasks. The memory photoconductivity is also modulated by X-ray intensity, as depicted in Figure 3E. We present the positive and negative polymorphic conductance variations of STM-PP and STM-NP under different X-ray dose rates (1.97 mGy s^{-1}, 3.93 mGy s^{-1}, 5.88 mGy s^{-1}, and 7.84 mGy s^{-1}) while maintaining a 10-s duration. The results indicate that higher dose rates result in larger memory currents over the same irradiation period. Figure 3F demonstrates the dependency of STM-PP and STM-NP on the X-ray dose rates. The detector's sensitivity is measured at 1,203 μC Gy^{-1} cm^{-2}, and both sensitivity and retention time remain unchanged after irradiation (Figures S15 and S16). As illustrated in Figure S17, 3-$APy_2BiBr_6 \cdot H_2O$ exhibits excellent X-ray attenuation capabilities, only slightly lower than those of common lead-based perovskite materials.

The preprocessing of images by the optic nerve in the human eye is crucial for enhancing the quality of sensory data. This process significantly boosts the efficiency and accuracy of subsequent tasks (image recognition and classification), facilitating the rapid capture of dynamic visual information.[19,31] In this investigation, the retina-mimicking X-ray detector is capable of emulating the functions of a biological retina, including sensing, memory, and processing. This is accomplished by convoluting a two-dimensional pixel matrix with both positive and negative conductance matrices. Enhancing image quality through advanced sensing data preprocessing can effectively emphasize important visual details, as evidenced by the subsequent image stylization process.[32,33] In our study, we developed an artificial neural network inspired by the functioning of the retina, utilizing an X-ray detector, as depicted in Figure 4A. The X-ray detector, designed to mimic the human retina, replicates both sensing and preprocessing functions. The refined image is then fed into a three-layer artificial neural network for image training and recognition purposes. This neural network comprises an input layer, a hidden layer, and an output layer,[34,35] as commonly seen in image recognition simulations.

The artificial neural morphology visual system utilizes a standard image database comprising images of moving objects within a container, such as blades, springs, and knives.[36] From this database, the target object, a blade, was selected as an example for demonstration, extracted from 400 images (Figure S20). The neural network is tasked with separating the target object from its surroundings.[37] Following preprocessing using the retina-mimicking X-ray detector, the essential information within the X-ray image is accentuated while redundant background signals are eliminated, as illustrated in Figure 4B. For our study, we utilized an L-shaped lead mask, 1 mm thick, as the object in the image. The mask dimensions were 8 × 12 mm^2, while each pixel measured 2 × 2 mm^2, as depicted in Figure S18. To ensure precise control over the detector movement and X-Y horizontal displacement, we employed a platform to drive an SC detector and manage the mask's motion. This setup enabled us to obtain X-ray images with the aid of auxiliary equipment (Figure S19).

Figure 4C illustrates the accuracy of target object classification with and without the retina-mimicking X-ray detector, revealing a notable enhancement in recognition rate and efficiency when using the latter. In the absence of retinomorphic X-ray detector preprocessing, the recognition rate can achieve 0.985 after 18 training epochs. However, with retinomorphic X-ray detector preprocessing, only 10 epochs are required to attain a recognition rate of 0.986. This highlights a significant improvement in image recognition efficiency due to the front-end image preprocessing. At the same time, preprocessing crucial information from the retinomorphic X-ray detector results in a more concentrated distribution of gray values within the image. This leads to increased image contrast and a compression ratio of 18.06% (Figure 4D). Such optimization substantially boosts the efficiency of data processing.

The recognition of the target object discussed above holds significant relevance across various applications in the X-ray detection field. This includes tasks like detecting foreign objects within sealed packaging (including blade detection images within the database) as well as in medical contexts. As an example, the retinomorphic X-ray detector could be utilized for monitoring blood movement, as depicted in Figure 4B, bottom. Following preprocessing, clear observation of blood circulation within the vessels becomes possible, facilitating real-time diagnosis, particularly in cases of heart disease. Additionally, in industrial settings, dynamic X-ray imaging plays a crucial role in the internal inspection of instruments, as shown in Figure S21.[38]

Conclusion

Our study introduced a novel class of X-ray detection materials capable of dual functions: X-ray detection and short-term memory. We successfully utilized these materials in motion-based intelligent X-ray detection projects, eliminating redundant and excessive information interaction. The retinomorphic X-ray detector demonstrates controllable short-term memory with positive and negative polarity (STM-PP and STM-NP), along with exceptional response linearity and long retention time. This innovative detection scheme seamlessly integrates X-ray perception, memory, and preprocessing into a single hardware unit, effectively tackling challenges related to data transmission, power consumption, and identification efficiency when compared to conventional X-ray detection methods. Furthermore, the findings emphasize the potential of reconfigurable halide perovskites for emerging computing paradigms and AI machines. The low-temperature and cost-effective preparation process further promotes the extensive adoption of perovskite materials in mainstream integrated circuit manufacturing.

MATERIALS AND METHODS

Materials preparation

3-APy (99%) was obtained from Macklin, while bismuth bromide ($BiBr_3$, 98%) and hydrobromic acid (48%) were acquired from Aladdin. Gold and platinum for thermal evaporation were received from Advanced Election Technology. PEDOT:PSS were obtained from Heraeus Group.

Preparation of 3-$APy_2BiBr_6 \cdot H_2O$ SCs

To synthesize 3-$APy_2BiBr_6 \cdot H_2O$, we initiated the process by gradually cooling the solution. First, we precisely measured 1 mmol of $BiBr_3$ powder within a glovebox. Subsequently, 2 mmol of 3-APy, in liquid form, equivalent to a solution volume of 200 μL, was added. The measured $BiBr_3$ and 3-APy were combined in a 10-mL glass container. Following this, 3 mL of hydrobromic acid was gradually introduced. The bottle neck was sealed with tape. The precursor solution was then immersed in an oil bath with an initial temperature of 120°C and maintained at this temperature for 6 h to ensure complete solubilization of the solute. During the cooling process, the temperature gradually decreased at a rate of 3 °C h^{-1} from 120°C to 100°C. As the crystallization temperature of the crystal was approximately 90°C, the cooling rate was then adjusted to 0.5 °C h^{-1} from 100°C to 80°C and subsequently maintained at 80°C.

Materials characterization

The XRD and SC-XRD analyses of the 3-$APy_2BiBr_6 \cdot H_2O$ X-ray memory detector were carried out using the X'PerT3 powder X-ray diffractometer (PANalytical) and XtaLAB PRO MM007HF Cu SC diffractometer (Rigaku). Elemental analysis was performed using an Elementar Vario EL cube instrument.

Device fabrication

We performed magnetron sputtering of MoO_3 (~10 nm) followed by the thermal evaporation of a Pt layer (55 nm) in sequence.

Detector performance measurement

To apply different bias voltages, we utilized the Keithley 6517B source meter. For evaluating X-ray detection performance, we employed the Amptek Mini-X2 tube with an Au target (Newton Scientific M237) as the X-ray source. Additionally, we utilized a horizontal displacement stage to move the samples in the X-Y direction. Dose rates were calibrated using accu-diode ionization chambers, including DDX6-W and DDX6-WL (Accu-Gold+, Radcal).

Imaging testing operation

The crystal samples were securely positioned on a displacement platform to ensure alignment of the mask, detector, and X-ray beam exit port at the initial pixel point. The detector was positively biased at 5 V. Upon activation of the Amptek Mini-X2 tube, we utilized the Keithley 6517B source meter to apply various bias voltages, enabling us to gather current information at the initial pixel point. Subsequently, the mask was adjusted to extract current information from another pixel point. The signals obtained were then summed and processed sequentially to generate the final output current at the initial pixel point. The platform was incrementally moved to capture imaging currents from the remaining pixel points, which were then pixelized.

REFERENCES

1. Sakdinawat, A., and Attwood, D. (2010). Nanoscale X-ray imaging. Nat. Photonics ***4***(12): 840–848. https://doi.org/10.1038/nphoton.2010.267.
2. Yaffe, M.J., and Rowlands, J.A. (1997). X-ray detectors for digital radiography. Phys. Med. Biol. ***42***(1): 1–39. https://doi.org/10.1088/0031-9155/42/1/001.
3. Huang, H., and Abbaszadeh, S. (2020). Recent developments of amorphous selenium-based X-ray detectors: a review. IEEE Sens. J. ***20***(4): 1694–1704. https://doi.org/10.1109/JSEN.2019.2950319.
4. Martz, H.E., Logan, C.M., Schneberk, D.J., et al. (2016). X-Ray Imaging: Fundamentals, Industrial Techniques and Applications (CRC Press).
5. Yabashi, M., and Tanaka, H. (2017). The next ten years of X-ray science. Nat. Photonics ***11***(1): 12–14. https://doi.org/10.1038/nphoton.2016.251.
6. Zentai, G. (2010). X-ray imaging for homeland security. Int J Signal Imaging ***3***(1): 13–20. https://doi.org/10.1504/IJSISE.2010.034628.
7. Thanki, R.M., and Ashish, K. (2019). Hybrid and Advanced Compression Techniques for Medical Images (Springer International Publishing).
8. Barman, R., Badade, S., Deshpande, S., et al. (2022). Lossless data compression method using deep learning. In Mach Intell Smart Syst, pp. 145–151. https://doi.org/10.1007/978-981-16-9650-3_11.
9. Withers, P.J., Bouman, C., Carmignato, S., et al. (2021). X-ray computed tomography. Nat. Rev. Methods Primers ***1***(1): 18. https://doi.org/10.1038/s43586-021-00015-4.
10. Anderson, D., and Trodden, J. (2013). USB 3.0 echnology (MindShare Press).
11. Masland, R.H. (2001). The fundamental plan of the retina. Nat. Neurosci. ***4***(9): 877–886. https://doi.org/10.1038/nn0901-877.
12. Grossniklaus, H.E., Geisert, E.E., and Nickerson, J.M. (2015). Introduction to the Retina. Prog Mol Biol Transl ***134***: 383–396. https://doi.org/10.1016/bs.pmbts.2015.06.001.
13. Nagarkar, V.V., Gupta, T.K., Miller, S.R., et al. (1998). Structured CsI (Tl) scintillators for X-ray imaging applications. IEEE T Nucl Sci ***45***(3): 492–496. https://doi.org/10.1109/23.682433.
14. Szeles, C. (2004). CdZnTe and CdTe materials for X-ray and gamma ray radiation detector applications. Phys. Status Solidi B ***241***(3): 783–790. https://doi.org/10.1002/pssb.200304296.
15. Zhang, H.T., Park, T.J., Islam, A.N.M.N., et al. (2022). Reconfigurable perovskite nickelate electronics for artificial intelligence. Science ***375***(6580): 533–539. https://doi.org/10.1126/science.abj7943.
16. Pan, C., Wang, C.Y., Liang, S.J., et al. (2020). Reconfigurable logic and neuromorphic circuits based on electrically tunable two-dimensional homojunctions. Nat. Electron. ***3***(7): 383–390. https://doi.org/10.1038/s41928-020-0433-9.

17. Menon, M., Mohammadi, S., Davila, J., et al. (2019). Single-cell transcriptomic atlas of the human retina identifies cell types associated with age-related macular degeneration. Nat. Commun. **10**(1): 4902. https://doi.org/10.1038/s41467-019-12780-8.
18. Sanyanusin, P., Schimmenti, L.A., Mcnoe, L.A., et al. (1995). Mutation of the PAX2 gene in a family with optic nerve colobomas, renal anomalies and vesicoureteral reflux. Nat. Genet. **9**(4): 358–364. https://doi.org/10.1038/ng0495-358.
19. Zhang, Z., Wang, S., Liu, C., et al. (2022). All-in-one two-dimensional retinomorphic hardware device for motion detection and recognition. Nat. Nanotechnol. **17**(1): 27–32. https://doi.org/10.1038/s41565-021-01003-1.
20. Zhuang, R., Wang, X., Ma, W., et al. (2019). Highly sensitive X-ray detector made of layered perovskite-like $(NH_4)_3Bi_2I_9$ single crystal with anisotropic response. Nat Photon **13**(9): 602–608. https://doi.org/10.1038/s41566-019-0466-7.
21. Zhou, Y., Zhao, L., Ni, Z., et al. (2021). Heterojunction structures for reduced noise in large-area and sensitive perovskite x-ray detectors. Sci. Adv. **7**(36): eabg6716. https://doi.org/10.1126/sciadv.abg6716.
22. Zhou, Y., Fei, C., Uddin, M.A., et al. (2023). Self-powered perovskite photon-counting detectors. Nature **616**(7958): 712–718. https://doi.org/10.1038/s41586-023-05847-6.
23. Wei, H., Fang, Y., Mulligan, P., et al. (2016). Sensitive X-ray detectors made of methylammonium lead tribromide perovskite single crystals. Nat Photon **10**(5): 333–339. https://doi.org/10.1038/nphoton.2016.41.
24. Jiang, Q., Tong, J., Xian, Y., et al. (2022). Surface reaction for efficient and stable inverted perovskite solar cells. Nature **611**(7935): 278–283. https://doi.org/10.1038/s41586-022-05268-x.
25. Huang, H.M., Yang, R., Tan, Z.H., et al. (2019). Quasi-hodgkin-huxley neurons with leaky integrate-and-fire functions physically realized with memristive devices. Adv. Mater. **31**(3): 1803849. https://doi.org/10.1002/adma.201803849.
26. Yin, H., Chen, Z., Peng, Y., et al. (2022). Dual active centers bridged by oxygen vacancies of ruthenium single-atom hybrids supported on molybdenum oxide for photocatalytic ammonia synthesis. Angew. Chem. Int. Ed. **61**(14): e202114242. https://doi.org/10.1002/anie.202114242.
27. Keene, S.T., Van der Pol, T.P.A., Zakhidov, D., et al. (2020). Enhancement-mode PEDOT:PSS organic electrochemical transistors using molecular de-doping. Adv. Mater. **32**(19): 2000270. https://doi.org/10.1002/adma.202000270.
28. Ma, Z., Shi, X.M., Nishimura, S., et al. (2022). Anhydrous fast proton transport boosted by the hydrogen bond network in a dense oxide-ion array of α-MoO_3. Adv. Mater. **34**(34): 2203335. https://doi.org/10.1002/adma.202203335.
29. Hu, S., Lozada-Hidalgo, M., Wang, F.C., et al. (2014). Proton transport through one-atom-thick crystals. Nature **516**(7530): 227–230. https://doi.org/10.1038/nature14015.
30. Cheng, X., Shen, S., Wei, G., et al. (2022). Perspectives on challenges and achievements in local oxygen transport of low Pt proton exchange membrane fuel cells. Adv Mater **7**(8): 2200228. https://doi.org/10.1002/admt.202200228.
31. Zhou, F., Zhou, Z., Chen, J., et al. (2019). Optoelectronic resistive random access memory for neuromorphic vision sensors. Nat. Nanotechnol. **14**(8): 776–782.
32. Wang, C.Y., Liang, S.J., Wang, S., et al. (2020). Gate-tunable van der Waals heterostructure for reconfigurable neural network vision sensor. Sci. Adv. **6**(26): eaba6173. https://doi.org/10.1126/sciadv.aba6173.
33. Gatys, L.A., Ecker, A.S., and Bethge, M. (2016). Image style transfer using convolutional neural networks. In Proc IEEE Conf Comput Vis Pattern Recognit, pp. 2414–2423.
34. Brady, T.F., Konkle, T., Alvarez, G.A., et al. (2008). Visual long-term memory has a massive storage capacity for object details. P Natl A Sci **105**(38): 14325–14329. https://doi.org/10.1073/pnas.0803390105.
35. Zhu, D., Li, Y., Shen, W., et al. (2017). Resistive random access memory and its applications in storage and nonvolatile logic. J. Semicond. **38**(7): 071002. https://doi.org/10.1088/1674-4926/38/7/071002.
36. Mery, D., Riffo, V., Zscherpel, U., et al. (2015). GDXray: The database of X-ray images for nondestructive testing. J. Nondestr. Eval. **34**(4): 42. https://doi.org/10.1007/s10921-015-0315-7.
37. Prezioso, M., Merrikh-Bayat, F., Hoskins, B.D., et al. (2015). Training and operation of an integrated neuromorphic network based on metal-oxide memristors. Nature **521**(7550): 61–64. https://doi.org/10.1038/nature14441.
38. Qiu, F., Peng, G., Xu, Y., et al. (2023). Sequential vacuum evaporated copper metal halides for scalable, flexible, and dynamic X-ray detection. Adv. Funct. Mater. **33**(36): 2303417. https://doi.org/10.1002/adfm.202303417.

ACKNOWLEDGMENTS

This work was supported by the National Natural Science Foundation of China (U23A20359), the Major State Basic Research Development Program of China (2021YFB3201000), the National Natural Science Foundation of China (62134003, 623B2033, and 62074066), the Natural Science Foundation of Hubei Province (2021CFA036, 2020CFA034), and the Shenzhen Science and Technology Program (SGDX20230116093205009). The authors would like to thank Wenxin Wang from Shiyanjia Lab (www.shiyanjia.com) for XRD analysis and Youwen Ren from SCI-GO (www.sci-go.com) for the rocking curve analysis.

AUTHOR CONTRIBUTIONS

G.N. conceived and supervised the project. H.Y. performed the growth of the single crystal, materials characterization, device fabrication, and demonstration for various applications. J.P. carried out the simulation of image stylization and construction of the artificial neural network. S.Z. completed the detector imaging. H.W. and Z.S. assisted with device optimization and data analysis. X.L., Z.Z., and L.X. provided the facility for X-ray detector measurements and some consultation. H.Y., G.N., and J.T. wrote the paper, and all authors commented on the manuscript.

DECLARATION OF INTERESTS

The authors declare no competing interests.

SUPPLEMENTAL INFORMATION

It can be found online at https://doi.org/10.1016/j.xinn.2024.100654.

LEAD CONTACT WEBSITE

http://faculty.hust.edu.cn/niuguangda/zh_CN/index.htm.